Enhanced superconductivity upon weakening of charge density wave transport in $2H$-TaS$_2$ in the two-dimensional limit

Yafang Yang,[1] Shiang Fang,[2] Valla Fatemi,[1] Jonathan Ruhman,[1] Efrén Navarro-Moratalla,[3] Kenji Watanabe,[4] Takashi Taniguchi,[4] Efthimios Kaxiras,[2,5] and Pablo Jarillo-Herrero[1,*]

[1]*Department of Physics, Massachusetts Institute of Technology, Cambridge, Massachusetts 02139, USA*
[2]*Department of Physics, Harvard University, Cambridge, Massachusetts 02138, USA*
[3]*Instituto de Ciencia Molecular, Universidad de Valencia, c/Catedrático José Beltrán 2, 46980 Paterna, Spain*
[4]*National Institute for Materials Science, Namiki 1-1, Tsukuba, Ibaraki 305-0044, Japan*
[5]*John A. Paulson School of Engineering and Applied Sciences, Harvard University, Cambridge, Massachusetts 02138, USA*

Layered transition-metal dichalcogenides that host coexisting charge-density wave (CDW) and superconducting orders provide ideal systems for exploring the effects of dimensionality on correlated electronic phases. Dimensionality has a profound effect on both superconductivity and CDW instabilities. Here we report a substantial enhancement of the superconducting T_c to 3.4 K for $2H$-TaS$_2$ in the monolayer limit, compared to 0.8 K in the bulk. In addition, the transport signature of a CDW phase transition vanishes in the two-dimensional limit. In our analysis of electronic and vibrational properties of this material, we show that a reduction of the CDW amplitude results in a substantial increase of the density of states at the Fermi energy, which can boost T_c by an amount similar to that seen in experiment. Our results indicate competition between CDW order and superconductivity in ultrathin $2H$-TaS$_2$ down to the monolayer limit, providing insight toward understanding correlated electronic phases in reduced dimensions.

I. INTRODUCTION

Transition-metal dichalcogenides (TMDs) $2H$-MX_2 (where $M =$ Nb, Ta and $X =$ S, Se) have attracted considerable attention as novel two-dimensional (2D) crystalline superconductors [1]. In these materials, superconductivity (SC) occurs in an environment of preexisting charge-density wave (CDW) order [2,3], making them an ideal platform to study many-body ground states and competing phases in the 2D limit. In bulk crystals, the reported critical temperature of the CDW transition decreases from 120 K in $2H$-TaSe$_2$ down to 30 K in $2H$-NbSe$_2$. Superconductivity weakens in approximately reverse order, with T_c increasing from around 0.2 K in $2H$-TaSe$_2$ to 7.2 K in $2H$-NbSe$_2$. The relationship between CDW and superconductivity in such systems is still under debate [4,5]. It is generally believed that their mutual interaction is competitive, but evidence to the contrary, indicating a cooperative interaction, has also been reported in angle-resolved photoemission spectroscopy (ARPES) studies [3].

In TMDs, superconductivity and CDW instability can be investigated by adjusting the interlayer interactions through pressure [6,7] or molecule intercalation [8,9]. Recently, mechanical exfoliation has emerged as a robust method for producing ultraclean, highly crystalline samples with atomic thickness [10]. This offers a useful way to assess the effect of dimensionality and interlayer interactions on both superconductivity and CDW. A material whose behavior as a function of layer thickness has been recently studied is NbSe$_2$ [11–14], in which the superconducting state is progressively weakened in samples thinner than five layers (5L), with T_c lowered from 7.2 K in bulk crystals to 3 K in the monolayer. The thickness dependence of CDW order is still under debate, with different results from Raman and scanning tunneling microscopy/spectroscopy (STM/STS) studies [15,16].

Bulk $2H$-TaS$_2$, another member of the $2H$-MX_2 family, exhibits a CDW transition at 70 K and a SC transition at 0.8 K [2,17–19]. Compared to NbSe$_2$, TaS$_2$ manifests a stronger signature of the CDW transition in transport in the form of a sharp decrease of resistivity [9], and thus serves as a desirable platform to study the thickness dependence of the CDW instability. STM/STS measurements on monolayer TaS$_2$ epitaxially grown on Au(111) substrates show suppression of the CDW instability [20]. Regarding superconductivity, an enhanced T_c down to a thickness of 3.5 nm (5L) was recently reported, utilizing TaS$_2$ flakes directly exfoliated on a Si/SiO$_2$ substrate [19]. Considering the fact that an appreciable decrease of T_c in NbSe$_2$ only occurs in samples thinner than five layers, it would be interesting to explore the trend of T_c in TaS$_2$ toward the exact 2D limit. Prior work found that samples thinner than 5L become insulating, indicative of its particular susceptibility to degradation in ambient atmosphere. Therefore, exfoliation and encapsulation in an inert atmosphere become crucial in order to obtain high-quality samples.

This paper is arranged as follows: in Sec. II, we report electronic transport studies of the properties of mono- and few-layer $2H$-TaS$_2$ at different temperatures and magnetic fields. We show that superconductivity persists in TaS$_2$ down to the monolayer limit, with a pronounced increase in T_c from

*pjarillo@mit.edu

0.8 K in bulk crystals to 3.4 K in the monolayer. At higher temperatures, two electronic transport signatures of the CDW transition are found to vanish in ultrathin samples: (1) a kink in the temperature dependence of the resistivity, and (2) a change of sign in the Hall coefficient versus temperature. In Sec. III, we report calculations on the electronic and vibrational properties to explore the competition between SC and CDW in this material. We found that suppression of the CDW order leads to a substantial increase in the density of states at the Fermi level, which ultimately enhances T_c. We also revisit the impact of quantum fluctuations of the CDW order on the enhancement of T_c. Our study provides insights into the importance of reduced dimensions on many-body ground states and their interactions.

II. EXPERIMENTAL RESULTS

A. Device fabrication

We exfoliate and fabricate samples with a transfer setup built inside a glovebox filled with argon gas, and encapsulate the TaS$_2$ flake between two sheets of hexagonal boron nitride (hBN). We build our devices utilizing a polymer pick-up technique [24] as illustrated in Fig. 1(a), taking advantage of the van der Waals adhesion between 2D layers. Using this technique, hBN and TaS$_2$ flakes are picked up in sequence and transferred onto preevaporated bottom contacts embedded in another hBN flake (see Appendix A for details). With this method, we minimize the exposure to ambient atmosphere during the device fabrication process, which makes it possible to produce high-quality TaS$_2$ samples as thin as monolayer in our experiment.

B. Enhanced superconductivity in the monolayer limit

As seen in Fig. 1(b), when the temperature is sufficiently low, a clear superconducting transition is observed for one-, two-, three-, five-, seven-layer, and bulk samples. By fitting the resistance to the Aslamazov-Larkin expression [25], we are able to determine the mean-field superconducting transition temperature T_c. When the sample thickness is decreased from bulk to monolayer, the corresponding T_c monotonically increases from 0.9 to 3.4 K [26]. The trend observed in our experiment is strictly opposite that of a previous finding on NbSe$_2$ [12], where T_c decreases monotonically with thickness reduction, despite the fact that the two materials are isostructural and isovalent. In NbSe$_2$, the decrease in T_c is attributed to a weaker interlayer Cooper pairing as the layer number N is reduced. In our case, however, it is surprising to see that even with a reduced interlayer Cooper pairing, the T_c is dramatically enhanced when the thickness is reduced. To verify that the thickness dependence of T_c is independent of extrinsic factors (such as level of disorder, substrate, source of crystal, sample quality), we measure an additional set of bilayer and trilayer samples and plot our results alongside previously reported T_c values [19] in Fig. 1(c). Independent of different sample preparation procedures and substrates, the trend of T_c versus thickness is consistent between the two sets of experimental results, indicative of an intrinsic origin underlying the enhancement of T_c.

To further characterize the superconducting properties of thin TaS$_2$, we measure the superconducting transition under
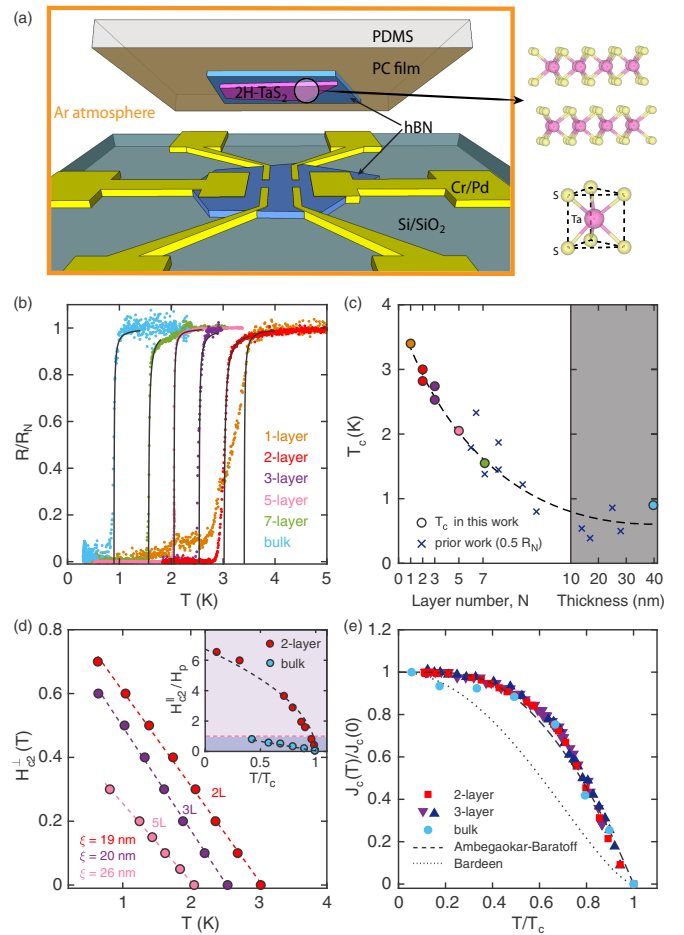

FIG. 1. (a) Schematic of device fabrication and crystal structure of 2H-TaS$_2$. (b) Resistance normalized by the normal state (R/R_N) as a function of temperature for one-, two-, three-, five-, seven-layer, and bulk ($d = 40$ nm) samples near the SC transition. The superconducting T_c is 3.4, 3.0, 2.5, 2.05, 1.6, and 0.9 K, respectively, determined by fitting the transition curve to the Aslamazov-Larkin formula (black solid lines). (c) T_c reported in this work (circles) and in a prior study (crosses) [19]. The dashed line guides the eye to the general trend. (d) Out-of-plane critical field H_{c2} for two-, three-, and five-layer samples. The dashed lines are linear fits to $H_{c2}^{\perp} = \phi_0/[2\pi\xi(0)^2](1 - T/T_c)$, where ϕ_0 and $\xi(0)$ denote the flux quantum and in-plane GL coherence length at zero temperature, respectively. Inset: In-plane critical field $H_{c2}^{\parallel}$ normalized by Pauli limit ($H_p \approx 1.86T_c$) for bilayer and bulk samples. The dashed line for the bilayer is a fit to the Tinkham formula [21] for 2D samples $H_{c2}^{\parallel} = \sqrt{12}\phi_0/[2\pi\xi(0)d]\sqrt{(1 - T/T_c)}$. The purple background indicates the Pauli limit regime. (e) Normalized critical current as a function of T/T_c. Dashed and dotted lines denote the models proposed by Bardeen [22] and Ambegaokar and Baratoff [23], respectively.

both out-of-plane and in-plane magnetic fields. Figure 1(d) shows the $H_{c2}^{\perp}$ as a function of temperature. Close to T_c, the dependence of $H_{c2}^{\perp}$ is fitted well by the phenomenological 2D Ginzburg-Landau (GL) model, which yields $\xi(0) =$ 19, 20, 26 nm for two-, three-, and five-layer respectively, where $\xi(0)$ denotes the GL coherence length at zero temperature. The reported values [27,28] for three dimensions range from 22 to 32.6 nm. For in-plane field, we observe a much
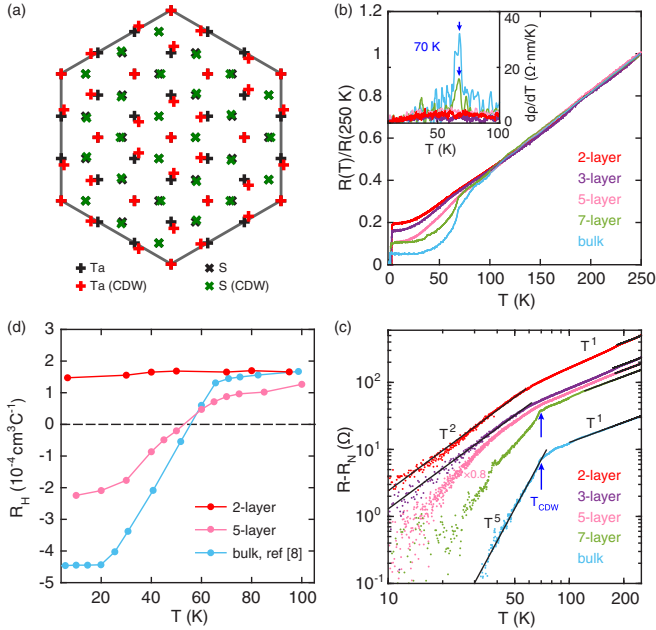
FIG. 2. (a) Illustration of the atom position of Ta and S atoms in the normal phase and the CDW phase. The periodicity of the CDW order is 3×3. (b) Normalized resistance $R(T)/R(250 \text{ K})$ for two-, three-, five-, seven-layer, and bulk samples, measured while cooling down. Inset: derivative of the resistivity $\rho = dR$ close to the CDW ordering temperature. An arrow is used to mark the T_{CDW} for bulk and seven layer, which both show a peak in $d\rho/dT$ at 70 K. (c) Resistance $R - R_N$ as a function of temperature plotted in a log-log scale, where R_N is the residual resistance just above the onset temperature of superconductivity. For clarity, data for five-layer is scaled by a factor of 0.8. (d) Hall coefficient $R_H = dV_H/(IB)$ measured while cooling down. Data for the bulk crystal is from Ref. [8].

larger $H_{c2}^{\parallel} = 32$ T at 300 mK for a bilayer ($T_c = 2.8$ K), which is more than six times the Pauli paramagnetic limit H_p, obeying a square root rather than a linear temperature dependence [inset of Fig. 1(d)]. This dramatic enhancement of in-plane $H_{c2}^{\parallel}$, often referred to as Ising superconductivity, has been observed in other 2D crystalline superconductors [12,13,29,30]. The above observations verify that thin TaS$_2$ behaves as a 2D superconductor. We also show that the superconducting transition exhibits the Berezinskii-Kosterlitz-Thouless (BKT) transition as expected in 2D in Appendix B. Additionally, the critical current density increases by orders of magnitude as the devices become thinner (bulk $J_c \approx 700$ A/cm^2, trilayer $J_c \approx 7 \times 10^5$ A/cm^2, bilayer $J_c \approx 1.2 \times 10^6$ A/cm^2). The trend of critical current density versus temperature for representative thicknesses is shown in Fig. 1(e), with a more detailed discussion given in Appendix C.

C. Transport properties and the CDW transition

In addition to the SC transition, bulk TaS$_2$ is known to exhibit CDW order below 70 K. The pattern of atomic displacements in the CDW state is illustrated in Fig. 2(a). In our experiment, we characterize the temperature-dependent resistance of two-, three-, five-, seven-layer, and bulk samples, and plot the normalized resistance versus temperature on a

linear scale in Fig. 2(b). All samples manifest a linear decrease of resistance at high temperatures, consistent with phonon limited resistivity in a normal metal [31]. Below 70 K, the seven-layer and bulk devices undergo a CDW phase transition, producing a kink in resistance, which is manifested as a peak in $d\rho/dT$. In the inset of Fig. 2(b), the temperature derivative of the resistivity is shown, and a peak in $d\rho/dT$ develops in seven-layer and bulk samples close to the transition. In two-, three-, and five-layer samples, however, such a peak in $d\rho/dT$ is absent.

To further investigate the temperature dependence of the sample resistance, we plot the subtracted resistance $R - R_N(4 \text{ K})$ on a log-log scale in Fig. 2(c). For bulk, the linear temperature dependence is disrupted by a sudden switch to T^5 near T_{CDW}, a well-known consequence of electron-phonon scattering at temperatures lower than the Debye temperature Θ_D. In contrast, a gradual transition to $R \sim T^2$ is observed in two- and three-layer samples. It is important to note that these powers are only observed over the range between $T \sim 55$ K and SC T_c and thus extend over a bit less than a decade.

In bulk TaS$_2$, the Hall coefficient undergoes a broad transition between 70 and 20 K including a change in sign at 56 K [8], which is another indicator of the electronic structure change induced by the CDW transition. It has been shown that a two-carrier model with light holes and heavy electrons is necessary to explain the opposite signs for the Seebeck and Hall coefficients measured above the CDW transition temperature, as opposed to a single-carrier model describing the low-temperature behavior [8]. In Fig. 2(d), we plot the Hall coefficient (R_H) of three representative thicknesses below 100 K. In the five-layer sample, a significant deviation from the bulk behavior is already apparent: the overall magnitude of R_H and temperature where it switches sign are both diminished. However, the most striking fact is the weak temperature dependence and absence of a sign change in the two-layer sample. This implies that the same electronic structure modification caused by the CDW transition that affects the Hall coefficient is also absent in the 2D limit.

III. DISCUSSION

As superconductors are thinned down to the 2D limit, their critical temperature T_c typically decreases [32]. This suppression of SC is normally attributable to either disorder-induced localization of Cooper pairs, weaker Coulomb screening in 2D, or reduction of the superfluid stiffness which leads to a reduction of the BKT transition temperature. Recent studies reveal more novel origins of suppressed superconductivity in atomically thin NbSe$_2$, including a weaker interlayer Cooper pairing [12] and suppression of the Cooper pair density at the superconductor-vacuum interface [14]. Beyond these mechanisms, here we consider a key factor affecting T_c that was not quantitatively studied in atomically thin layered $2H$-MX_2: the interaction with CDW order.

Anticorrelated trends between SC and CDW transition have been observed in bulk $2H$-TaS$_2$ crystals under pressure [6,28] and in single-crystal alloys [33–35]. Here we hypothesize that the enhancement of T_c as sample thickness decreases all the way to the 2D limit is associated with a suppression of the electronic structure reconstruction induced by the CDW order.
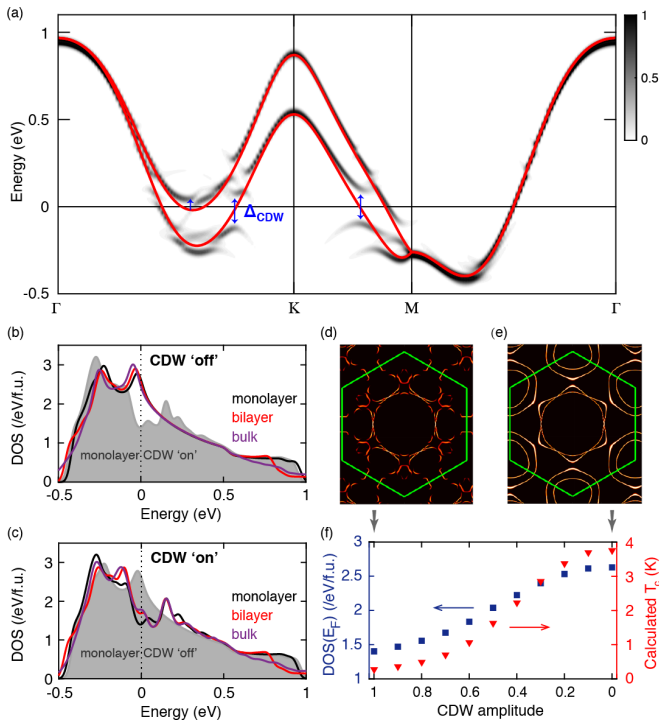
FIG. 3. (a) Band structure for monolayer $2H$-TaS$_2$. The gray lines show the unfolded band structure compared with the original band structure in the normal phase (red lines). (b) Density of states for monolayer/bilayer/bulk in the normal phase. Monolayer in the CDW phase is plotted as a gray shade for reference. (c) Density of states for monolayer/bilayer/bulk in the CDW phase. Monolayer in the normal phase is plotted as a gray shade for reference. (d) Energy contour at the Fermi energy in the CDW phase for monolayer TaS$_2$. (e) Energy contour at the Fermi energy in the normal phase for monolayer TaS$_2$. (f) Left axis: density of states at the Fermi level DOS(E_F) as a function of CDW amplitude for the monolayer. Right axis: T_c from McMillan's formalism [45] using the calculated DOS(E_F).

To better understand the possible interplay between the SC and CDW transitions, we investigate the electronic and vibrational properties of $2H$-TaS$_2$ with density functional theory (DFT), as implemented in the VASP code [36,37], which allows us to obtain the density of states (DOS) in the normal and the CDW phases for monolayer, bilayer, and bulk. A comparison of Figs. 3(b) and 3(c) reveals an appreciable reduction of DOS near the Fermi level induced by CDW order for all three thicknesses. This is consistent with previous magnetic susceptibility and heat capacity experiments showing a sharp drop of density of states below the CDW transition [38,39].

We investigate next the effects of CDW on the band structure. In Fig. 3(a), we plot the band structures in the normal phase and in the CDW phase, denoted by red and gray curves. In order to display the band structure of the CDW phase in the original Brillouin zone (BZ), we need to "unfold" the calculated CDW band structure from the supercell BZ (sBZ) to the original BZ. This is achieved by performing a Wannier transformation [40] to decompose the extended Bloch wave functions onto localized atomic orbitals from the tight-binding Hamiltonian [41,42] (see Appendix E for more details). It is clearly seen in Fig. 3(a) that the CDW distortions result in a gap

forming on the inner pocket around K along Γ-K and K-M. In addition, the saddle point located along Γ-K, is shifted to energies above the Fermi level. The reconstruction of electronic structures induced by the CDW order is also seen in the Fermi energy contour plots shown in Figs. 3(d) and 3(e). After the CDW transition, the pockets around K and Γ are either partially or fully gapped. This reconfiguration of electronic structures may account for the abnormal change of sign seen in the Hall measurement. However, a quantitative analysis is not possible without access to both the local curvature of the Fermi surface and the anisotropy in the scattering time at different k points. Given that the k-dependent CDW-gap and SC-gap formation in $2H$-MX_2 have been intensively studied by ARPES [3,43], our DFT calculations can serve as a check of these results.

We also computed the phonon dispersion for the bulk and monolayer (see Appendix F). We find that in both cases, an acoustic mode that involves in-plane motion of Ta atoms softens and becomes unstable as the electronic temperature is lowered. In both cases the instability occurs at approximately the same wave vector that corresponds to the CDW ordering $Q_{\mathrm{CDW}} \approx 2/3 \Gamma M$ [44]. This is in good agreement with the 3×3 periodicity of the CDW order observed in $2H$-MX_2.

To investigate the change of T_c that may be induced by a suppression of the CDW order, we calculate T_c as a function of CDW amplitude based on electronic and phononic structure calculations. We recall that in McMillan's theory, the critical temperature is expressed as [45]

$$T_c = \frac{\Theta_D}{1.45} \exp\left[-\frac{1.04(1+\lambda)}{\lambda - \mu^*(1+0.62\lambda)}\right], \qquad (1)$$

where μ^* is the Coulomb pseudopotential of Morel and Anderson, and λ is the electron-phonon coupling constant. We find that if the CDW distortion is completely suppressed, the corresponding change in DOS(E_F) can result in an enhancement of T_c up to 3.75 K (see Appendix G). The result is summarized in Fig. 3(f). This provides a good approximate estimate on the impact of the suppression of the CDW instability on the superconducting T_c. Interestingly, this estimate agrees reasonably well with our experiment, indicating the importance of including electronic structure modifications induced by the CDW as a contributing factor. We note that there are several other factors that can impact T_c, such as substrate effects, the presence of a van Hove singularity near the Fermi level, and enhanced electron-phonon coupling due to reduced screening [19] in 2D. These factors have been discussed in great detail in the literature and we do not reiterate them here.

The above analysis investigates primarily the direct competition between CDW and superconductivity over DOS. We further note that a continuous suppression of the CDW phase as a function of thickness would imply a softening of the CDW amplitude mode. If the presence of quantum fluctuations caused by proximity to a CDW transition is considered, the analysis of its impact on SC can go beyond a simple "competing order" scenario [46]. The competition between fermionic incoherence and the strong electron-mediated pairing near a quantum critical point can yield a pairing instability at temperature T_c which increases and saturates as the order correlation length $\xi \to \infty$. This reveals potentially rich relationships between CDW and SC that cannot be simply interpreted in the

BCS framework as the material thickness is reduced toward the 2D limit.

After careful analysis of possible correlations between SC and CDW in TaS_2 by DFT calculations, we turn to a discussion on the transport data shown in Sec. II C. We will argue that the transport data is also consistent with the scenario of suppression of the CDW transition as sample thickness decreases. Let us start from the disappearance of the kink in the resistivity curve in Fig. 2(a). While the exact relation between the CDW ordering and the kink is not fully understood, its disappearance is definitely consistent with suppression of the CDW transition temperature or a complete disappearance of the ordering phase. The evolution of this kink was also studied in bulk samples of TaS_2 with intercalation, showing similar disappearance of the kink when the CDW order is suppressed [8]. The change in the power of the temperature-dependent resistivity from T^5 to T^2 can also be explained within the same framework. However, in this case it is only consistent if the suppression of the CDW order is continuous, such that the gap of the amplitude mode of the CDW becomes very small in ultrathin samples. As we show in the Supplemental Material [47], when the gap of the amplitude mode is smaller than thermal excitations, scattering of electrons off these fluctuations leads to a strong T^2 contribution to the resistivity [48]. We also note that using a Kadawaki-Woods scaling [49] one finds that the T^2 resistivity from electron-electron scattering is expected to be much smaller than the one we measured. Finally, the absence of a change in the sign of the Hall coefficient indicates that the change in electronic structure occurring in the bulk is either absent or different in the 2D limit. Thus, it could be that the CDW order disappears, or a different type of CDW order is stabilized in the ultrathin limit. In summary, we find that both the superconducting and transport data are consistent with the hypothesis that the CDW order is continuously suppressed when reducing the sample thickness toward the 2D limit. It is, however, important to point out that none of our probes directly measure such an effect and at this point it can only be viewed as a hypothesis consistent with multiple different measurements.

IV. CONCLUSION

We observe enhanced superconductivity in atomically thin $2H$-TaS_2 accompanied with suppression of the CDW-induced transport signatures. Our electronic band structure calculations show that suppression of the CDW phase leads to a substantial increase in $DOS(E_F)$, which acts to boost the superconducting T_c. Our result reveals that competition of the two ordered phases in determining the DOS can provide a reasonable explanation of the enhanced superconducting T_c in this material down to the monolayer limit. Future layer-dependent studies that directly probe the CDW order, for example, through STM/STS, Raman, and ultrafast spectroscopy measurements, will be essential to understanding the origin of the CDW formation and its stability against dimensional reduction. Future studies on the microscopic origin of the mechanisms (electronic, magnetic, electron-phonon, etc.) will be of paramount importance to a comprehensive understanding of the mutual interactions between the CDW and SC.

Note added. Recently, we became aware of a related work [50].

APPENDIX A: SAMPLE PREPARATION

The sample fabrication process takes place in a glovebox filled with argon gas. TaS_2 crystals (from HQgraphene) are exfoliated onto Si/SiO_2 wafers inside the glovebox. hBN flakes that support bottom contacts are exfoliated onto Si/SiO_2 wafers. Wafers with hBN flakes are then annealed in Ar/H_2 atmosphere at $350\,°C$ for 3–5 hours. Selected hBN flakes, with thickness ranging from 20 to 30 nm, are patterned with e-beam lithography using MMA/ZEP followed by XeF_2 gas etch for $20\,s \times$ five cycles. Then Cr/Pd 2/25 nm is evaporated by thermal or e-beam deposition. In this way, bottom contacts that are embedded in hBN are fabricated. Using a slide consisting of a poly(bisphenol A carbonate) film held on top of a piece of polydimethylsiloxane (PDMS) elastomer, hBN and TaS_2 flakes can be picked up in sequence and transferred onto the bottom contacts. Such encapsulation allows for a van der Waals seal between two hBN flakes and therefore prohibits exposure to air during the sample transportation outside the glovebox.

APPENDIX B: BKT TRANSITIONS

In 2D superconductors, when $d < \xi(0)$ and the lateral size is smaller than the in-plane magnetic penetration length ($\lambda_{ab} = \lambda^2/d$, estimated to be $\sim 30\,\mu m$ in thin-layer $2H$-TaS_2, assuming $\lambda = 210$ nm and $d = 1.4$ nm [27]), the SC transition is expected to be of the BKT type [51]. In BKT theory, when the temperature drops below the Bardeen-Cooper-Schrieffer (BCS) mean-field transition temperature T_c, a loss of global phase coherence and dissipation due to a finite flux resistance
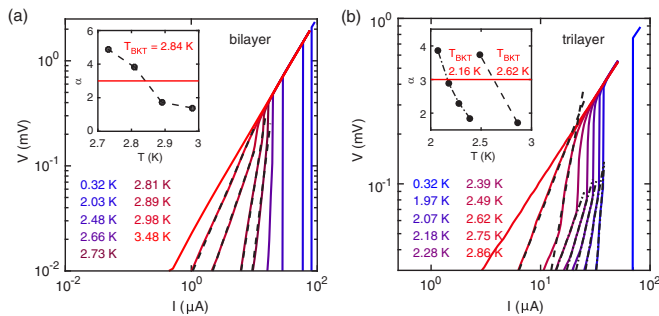
FIG. 4. Characterization of the BKT transition of (a) bilayer and (b) trilayer samples by measuring voltage-current behavior at various temperatures. Inset shows the exponent α versus T extracted from power-law fitting $V \propto I^{\alpha}$ near the BKT transition. The transition temperature T_{BKT} is obtained when the exponent α passes through 3.

occur with thermally excited vortices. In this regime, a finite supercurrent can flow below the BKT transition temperature T_{BKT}, as a consequence of formation of bound vortex-antivortex pairs. Experimentally, T_{BKT} can be determined by analyzing the I-V characteristic curves at various temperatures, expected to manifest a universal relation $V \propto I^3$ when vortex-antivortex pairs dissociate. I-V analysis for a bilayer ($T_c = 3$ K) and another trilayer ($T_c = 2.78$ K) sample is shown in Fig. 4, where voltage obeys nonlinear current dependence $V \propto I^{\alpha}$ during the BKT transition. By plotting the voltage-current data in a log-log scale and fitting the slope to α, we can get α as a function of temperature (shown in inset of Fig. 4). In this way, we estimate T_{BKT} as when α crosses the value of 3. T_{BKT} is found to be 2.8 and 2.6 K for bilayer and trilayer, respectively. They are close to and slightly lower than the BCS mean field T_c measured with $R(T)$ curves, which is also consistent with the BKT theory. Here we note that there might be inhomogeneity in this trilayer sample, which shows two sections of upturning voltages, possibly due to vortex pinning by a selected disordered region.

APPENDIX C: CRITICAL CURRENT

In Fig. 1(e), it is remarkable that all the critical current data collapse into a single trace. By analysis of this curve, we observe that it clearly deviates from the GL theory [21], which predicts that J_c is proportional to $(1 - T/T_c)^{3/2}$. In addition, we compare our result with Bardeen's phenomenological expression [22] $J_c(T)/J_c(0) = [1 - (T/T_c)^2]^{3/2}$ [dotted line in Fig. 1(e)], which is an approximation of numerical calculations based on dirty-limit microscopic theory that extends the GL theory to low temperatures. There is still a discrepancy between our result and Bardeen's model. Ambegaokar and Baratoff [23] then proposed that if the system comprises of superconducting grains connected with an insulating region, the maximum dc Josephson current is expressed as

$$I_0(T) = [\pi \Delta(T)/2eR_N] \tanh [\Delta(T)/2k_BT], \quad \text{(C1)}$$

where $\Delta(T)$ is the temperature-dependent BCS gap parameter and R_N is the normal-state tunneling resistance of a junction. Among the aforementioned models, the Ambegaokar-Baratoff model fits best with our experimental data.
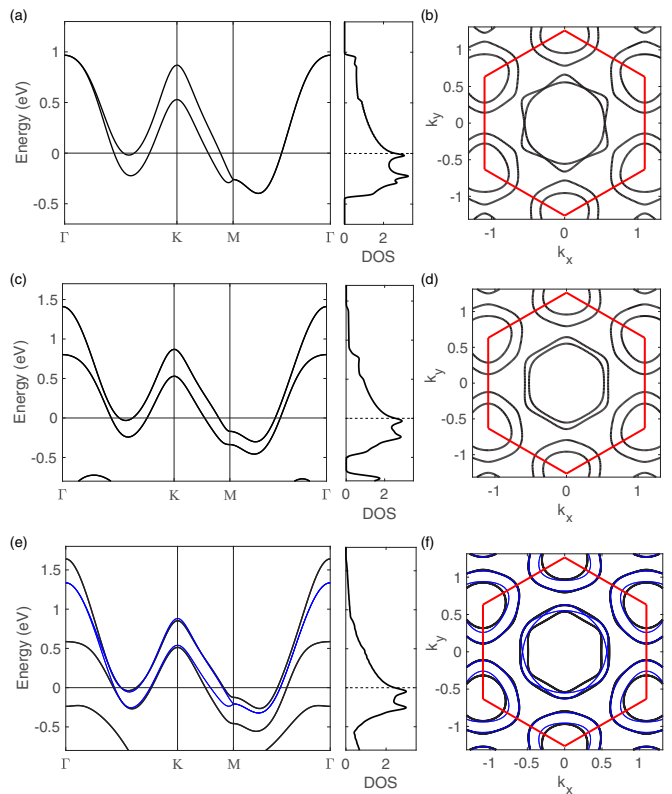

FIG. 5. Electronic band structure with spin-orbit coupling along Γ-K-M-Γ and the corresponding density of states (number of electrons/eV/f.u.) for TaS_2 crystals of the (a) monolayer, (c) bilayer, and (e) bulk form (black lines for $k_z = 0$ and thinner blue lines for $k_z = \pi$). The density of states here contains contributions from all bands. The corresponding energy contour at the Fermi level with Brillouin zone delineated by the red hexagon for the (b) monolayer, (d) bilayer, and (f) bulk cases (the black thick lines are the energy contours with $k_z = 0$ while the thinner blue lines are for contours with $k_z = \pi$).

APPENDIX D: ELECTRONIC BAND STRUCTURE FOR PRISTINE CRYSTALS

$2H$-TaS_2 and the TMD family exhibit a trigonal prismatic structure, in which the Ta atoms in all the layers are aligned vertically but the S sublattice is rotated by $60°$ with respect to that of the neighboring layer. In the simplest monolayer structure with spin-orbit coupling, the relevant group of bands near the Fermi level are 22 bands that are mostly composed of the d orbitals of Ta atoms and the p orbitals of S atoms. Thus, we include all these relevant p-d orbital hybrids in deriving the Wannier tight-binding Hamiltonians. Due to the broken inversion symmetry, spin splitting in the bands from spin-orbit coupling is present at generic k points. To give the essential physics picture and elucidate the features in the electronic structure, here we provide more electronic structure details for the pristine monolayer, bilayer, and bulk crystals. In Fig. 5, we summarize the band plots along Γ-K-M-Γ, density of states, and the energy contour at the Fermi energy. We find that the Fermi contour and the DOS at the Fermi level in the monolayer are not very different from the bulk case. Therefore band structure modification due to reduction of dimensionality
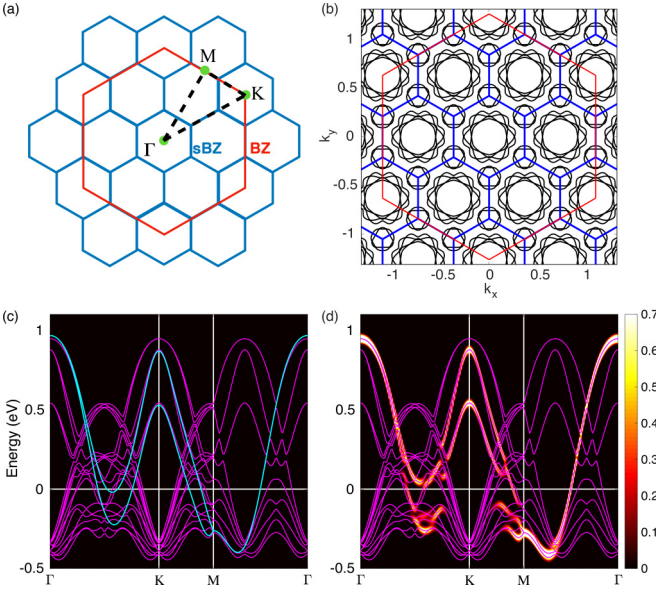
FIG. 6. CDW-ordered monolayer electronic band structure, the folding effects from the supercell geometry, and the inverse unfolding process. (a) BZ (red hexagon) and sBZ (blue hexagons) in the repeated zone. (b) Energy contour of the CDW-ordered monolayer crystal in the repeated zone scheme (contrast with the ones for the pristine crystal without CDW order in Fig. 5). (c) Folded CDW band structure (magenta) along Γ-K-M-Γ as outlined in (a). For comparison, bands from the pristine crystal without CDW order in the 1×1 unit cell are also plotted (cyan). (d) Folded supercell bands (magenta) compared with the unfolded and weighted effective bands. The unfolded effective bands differ from the pristine electronic band structure by additional features such as gap opening from CDW perturbations [as in Fig. 3(a)]. The Fermi level is indicated by the white horizontal line. When the CDW energy contour in (b) is decorated with the unfolding weight as the band structure, the unfolded CDW energy contour is obtained in Fig. 3(d).

itself cannot result in the enhancement of T_c. More details and numerical implementations can be found in the Supplemental Material [47].

APPENDIX E: ELECTRONIC BAND STRUCTURE UNFOLDING

The CDW phase leads to a deformed crystal lattice as shown in Fig. 2(a) with 3×3 periodicity, whose band structure can be plotted in a supercell Brillouin zone. It can be viewed as the "folded" bands from the original bands of the pristine crystal. We describe here the details for the reverse "unfolding" procedure [41,52,53], which aims to present the CDW effects as perturbation on the pristine band structure.

When the primitive unit cell in real space is enlarged to the supercell, the corresponding BZ in the reciprocal space is shrunk to the sBZ. In Fig. 6(a), we compare in reciprocal space the original BZ (red hexagon) and the sBZ (blue hexagons) in the repeated zone scheme. We use $\vec{a}_i$ to denote the primitive vectors of the original 1×1 unit cell, and $\vec{a}_i^{SC} = 3\vec{a}_i$ for the 3×3 supercell primitive vectors. The corresponding reciprocal lattice vectors are $\vec{G}_i$ and $\vec{G}_i^{SC} = \vec{G}_i/3$. The area of one original BZ contains nine sBZs. Suppose the crystal

momentum $\vec{k}^{SC}$ lies within sBZ; any crystal momentum $\vec{k} = \vec{k}^{SC} + p_1\vec{G}_1^{SC} + p_2\vec{G}_2^{SC}$ with integers p_i in original BZ would be classified as the same $\vec{k}^{SC}$ in the sBZ (repeated zone). This can be seen from the Bloch theorem derived from the translational symmetry under the supercell translation vectors $\vec{T}^{SC} = m_1\vec{a}_1^{SC} + m_2\vec{a}_2^{SC}$ with integers m_i.

$$e^{i\vec{k}\cdot\vec{T}^{SC}} = e^{i(\vec{k}^{SC}+p_1\vec{G}_1^{SC}+p_2\vec{G}_2^{SC})\cdot(m_1\vec{a}_1^{SC}+m_2\vec{a}_2^{SC})} \tag{E1}$$

$$= e^{i\vec{k}^{SC}\cdot(m_1\vec{a}_1^{SC}+m_2\vec{a}_2^{SC})} \tag{E2}$$

$$= e^{i\vec{k}^{SC}\cdot\vec{T}^{SC}} \tag{E3}$$

for distinct p_i integers. Various crystal momentum states in the original 1×1 unit cell description are thus mapped onto the "folded" $\vec{k}^{SC}$ crystal momentum label in the supercell description. The perturbation from CDW deformation introduces coupling and mixing between these momentum states. Because the states and bands are folded in the sBZ, for each $\vec{k}^{SC}$ there are nine times the number of bands in the sBZ than the original BZ description. In the repeated sBZ scheme, the energy contour at Fermi energy for the monolayer with CDW is shown in Fig. 6(b). The topography of the energy contour from the band folding is substantially more complicated than that of the pristine crystal without CDW, shown in Fig. 5. The band structure in Fig. 6(c) along the momentum line as in Fig. 6(a) also shows the supercell bands that are drastically different from those of the pristine crystal.

As shown in Fig. 5, the band folding can be traced back to the associated phase factor and the crystal momentum of the Bloch theorem. Within the supercell description, the crystal momentum $\vec{k}^{SC}$ is defined under the supercell translation $\vec{T}^{SC}$. As a result, the translational properties under the smaller original primitive vectors are not resolved with the $\vec{k}^{SC}$ supercell crystal momentum labeling. Any state with $\vec{k} = \vec{k}^{SC} + p_1\vec{G}_1^{SC} + p_2\vec{G}_2^{SC}$ (original crystal momentum defined with translation $\vec{T}$ spanned by primitive vector $\vec{a}_i$) is compatible with the supercell crystal momentum $\vec{k}^{SC}$, with the same reasoning as in Eq. (E1). However, in many cases such as CDW order, there is weak translational symmetry breaking, and the translational symmetry for the 1×1 unit cell can be treated as the approximate symmetry of the crystal. That is, we can decompose a supercell Bloch state or an energy eigenstate at $\vec{k}^{SC}$ into components with distinct translational properties under the original $\vec{T}$ and label them with $\vec{k} = \vec{k}^{SC} + q_1\vec{G}_1^{SC} + q_2\vec{G}_2^{SC}$:

$$\psi_{\vec{k}}^{SC} = \sum_{\vec{k}'=\vec{k}+p_1 G_1^{SC}+p_2 G_2^{SC}} \psi_{\vec{k}'}, \tag{E4}$$

which has nine components in the 3×3 supercell. In the perturbative regime, we can start with the pristine crystal without CDW order and the translational symmetry under $\vec{T}$ is recovered. This translation symmetry eliminates the mixings between distinct $\vec{k}'$ components classified under the same supercell $\vec{k}^{SC}$. CDW order breaks the $\vec{T}$ translation symmetry and induces mixing between $\vec{k}'$ components. To compare and contrast with the original pristine crystal band structure in the repeated zone scheme, the $\psi_{\vec{k}'=\vec{k}}$ component is singled out and the unfolding weight for the state is defined as the norm of this specific component $|\psi_{\vec{k}'}|^2$. When the supercell band structure is
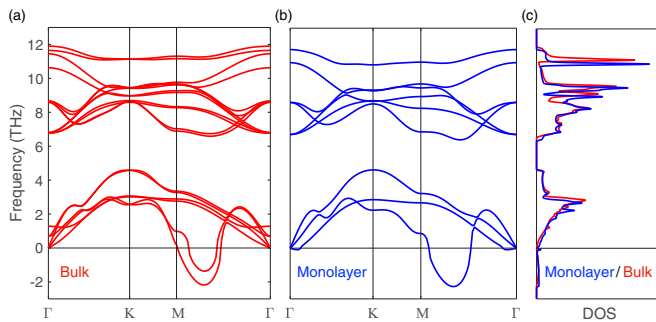
FIG. 7. Phonon spectrum along Γ-K-M-Γ for TaS$_2$ (a) bulk and (b) monolayer crystals. (c) The comparisons of the density of states of the monolayer (blue) and the bulk (red) crystals.

plotted with the unfolding weight for each state as in Fig. 6(d), the band structure with weights is greatly simplified and they are defined as the unfolded band structure. These unfolded and weighted bands are then compared with the pristine bands without CDW in Fig. 3(a). Clearly, these unfolded CDW bands introduce additional electronic features to the pristine band structure such as the splittings and the gap opening from CDW order. The same unfolding procedure can also be applied to the Fermi energy contour change due to CDW as in Fig. 3(d).

The unfolded band structure can be compared with the band structure from the ARPES measurements. The same unfolding scheme can also be applied to the cases of impurities in the crystal [42] or disordered solids [54], and Fe-based high-temperature superconductors [53]. When the perturbation terms in these cases are added to the system gradually, the unfolded bands with weights also change perturbatively from the original ones. The effective band structures are a more natural and intuitive way of generalizing the conventional band structure and comparing with experiment in these cases even though the translation symmetries of the primitive cell are broken.

APPENDIX F: PHONON DISPERSION

For TaS$_2$ crystals, the phonon properties are calculated within density functional perturbation theory, using the VASP code with the PHONOPY package [55]. A $6 \times 6 \times 2$ ($8 \times 8 \times 1$) supercell geometry is employed for the bulk (monolayer) crystal, with the calculated phonon spectrum and the density of states shown in Fig. 7. We find that the average phonon frequency slightly decreases for the monolayer case, with squared phonon frequency $\langle \omega^2 \rangle$ changing from 58.12 THz^2 in bulk to 56.59 THz^2 in monolayer.

APPENDIX G: McMILLAN'S FORMALISM

In McMillan's theory [45], the critical temperature is expressed by Eq. (1), where μ^* is the Coulomb pseudopotential of Morel and Anderson given by

$$\mu^* = \frac{\text{DOS}(E_F)\langle V_c \rangle}{1 + \text{DOS}(E_F)\langle V_c \rangle \ln\left(\frac{E_B}{\omega_0}\right)}, \tag{G1}$$

and λ is the electron-phonon coupling constant

$$\lambda = \text{DOS}(E_F)\langle I^2 \rangle / M \langle \omega^2 \rangle \tag{G2}$$

with $\text{DOS}(E_F)$ the density of states, V_c the matrix element of the screened Coulomb interaction, E_B the electronic bandwidth, ω (ω_0) the (maximum) phonon frequency, I the electron-phonon matrix elements, M the atom mass, and $\langle \cdots \rangle$ the average over the Fermi surface. Assuming $\mu^* = 0.15$ as suggested by McMillan, one can evaluate the inverted form of the above equation and obtain $\lambda = 0.482$ for TaS$_2$ by assuming $\Theta_D = 250$ K [56] and $T_c = 0.8$ K [19], indicating that TaS$_2$ lies in the intermediate coupling regime.

We then investigate the impact of progressive weakening of the CDW by varying the magnitude of atomic distortion. A scaling factor, from 1 to 0, is used to define the fraction by which the magnitude of the atomic displacement is reduced with respect to the stable distorted configuration. The corresponding DOS as a function of atom displacement amplitude is calculated by DFT. Using the bulk as a starting point, we take into account the change in $\text{DOS}(E_F)$ and a small phonon energy shift $\langle \omega^2 \rangle$ calculated for the monolayer, and predict T_c within the McMillan formalism.

[1] Y. Saito, T. Nojima, and Y. Iwasa, Nat. Rev. Mater. **2**, 16094 (2016).

[2] A. H. Castro Neto, Phys. Rev. Lett. **86**, 4382 (2001).

[3] T. Kiss, T. Yokoya, A. Chainani, S. Shin, T. Hanaguri, M. Nohara, and H. Takagi, Nat. Phys. **3**, 720 (2007).

[4] M. Calandra, I. I. Mazin, and F. Mauri, Phys. Rev. B **80**, 241108 (2009).

[5] Y. Ge and A. Y. Liu, Phys. Rev. B **86**, 104101 (2012).

[6] D. Freitas, P. Rodiere, M. Osorio, E. Navarro-Moratalla, N. Nemes, V. Tissen, L. Cario, E. Coronado, M. García-Hernández, S. Vieira *et al.*, Phys. Rev. B **93**, 184512 (2016).

[7] C. W. Chu, V. Diatschenko, C. Y. Huang, and F. J. DiSalvo, Phys. Rev. B **15**, 1340 (1977).

[8] A. Thompson, F. Gamble, and R. Koehler, Jr., Phys. Rev. B **5**, 2811 (1972).

[9] J. A. Wilson, F. Di Salvo, and S. Mahajan, Adv. Phys. **24**, 117 (1975).

[10] A. K. Geim and K. S. Novoselov, Nat. Mater. **6**, 183 (2007).

[11] Y. Cao, A. Mishchenko, G. Yu, E. Khestanova, A. Rooney, E. Prestat, A. Kretinin, P. Blake, M. Shalom, C. Woods *et al.*, Nano Lett. **15**, 4914 (2015).

[12] X. Xi, Z. Wang, W. Zhao, J.-H. Park, K. T. Law, H. Berger, L. Forró, J. Shan, and K. F. Mak, Nat. Phys. **12**, 139 (2016).

[13] A. W. Tsen, B. Hunt, Y. D. Kim, Z. J. Yuan, S. Jia, R. J. Cava, J. Hone, P. Kim, C. R. Dean, and A. N. Pasupathy, Nat. Phys. **12**, 208 (2016).

[14] E. Khestanova, J. Birkbeck, M. Zhu, Y. Cao, G. L. Yu, D. Ghazaryan, J. Yin, H. Berger, L. Forró, T. Taniguchi, K. Watanabe *et al.*, Nano Lett. **18**, 2623 (2018).

[15] X. Xi, L. Zhao, Z. Wang, H. Berger, L. Forró, J. Shan, and K. F. Mak, Nat. Nanotechnol. **10**, 765 (2015).

[16] M. M. Ugeda, A. J. Bradley, Y. Zhang, S. Onishi, Y. Chen, W. Ruan, C. Ojeda-Aristizabal, H. Ryu, M. T. Edmonds, H.-Z. Tsai *et al.*, Nat. Phys. **12**, 92 (2016).

[17] S. Nagata, T. Aochi, T. Abe, S. Ebisu, T. Hagino, Y. Seki, and K. Tsutsumi, J. Phys. Chem. Solids **53**, 1259 (1992).

[18] I. Guillamón, H. Suderow, J. G. Rodrigo, S. Vieira, P. Rodière, L. Cario, E. Navarro-Moratalla, C. Martí-Gastaldo, and E. Coronado, New J. Phys. **13**, 103020 (2011).

[19] E. Navarro-Moratalla, J. O. Island, S. Mañas-Valero, E. Pinilla-Cienfuegos, A. Castellanos-Gomez, J. Quereda, G. Rubio-Bollinger, L. Chirolli, J. A. Silva-Guillén, N. Agraït, G. A. Steele, F. Guinea, H. S. J. van der Zant, and E. Coronado, Nat. Commun. **7**, 11043 (2016).

[20] C. E. Sanders, M. Dendzik, A. S. Ngankeu, A. Eich, A. Bruix, M. Bianchi, J. A. Miwa, B. Hammer, A. A. Khajetoorians, and P. Hofmann, Phys. Rev. B **94**, 081404 (2016).

[21] M. Tinkham, *Introduction to Superconductivity* (Dover, New York, 2004).

[22] J. Bardeen, Rev. Mod. Phys. **34**, 667 (1962).

[23] V. Ambegaokar and A. Baratoff, Phys. Rev. Lett. **10**, 486 (1963).

[24] J. I.-J. Wang, Y. Yang, Y.-A. Chen, K. Watanabe, T. Taniguchi, H. O. Churchill, and P. Jarillo-Herrero, Nano Lett. **15**, 1898 (2015).

[25] L. Aslamasov and A. Larkin, Phys. Lett. A **26**, 238 (1968).

[26] For the monolayer flake, determination of T_c becomes tricky due to electrical shortage to adjacent flakes with different thickness. Detailed analysis and determination of T_c by critical current mapping can be found in the Supplemental Material [47].

[27] Y. Kashihara, A. Nishida, and H. Yoshioka, J. Phys. Soc. Jpn. **46**, 1112 (1979).

[28] M. Abdel-Hafiez, X.-M. Zhao, A. Kordyuk, Y.-W. Fang, B. Pan, Z. He, C.-G. Duan, J. Zhao, and X.-J. Chen, Sci. Rep. **6**, 31824 (2016).

[29] J. Lu, O. Zheliuk, I. Leermakers, N. F. Yuan, U. Zeitler, K. T. Law, and J. Ye, Science **350**, 1353 (2015).

[30] Y. Saito, Y. Nakamura, M. S. Bahramy, Y. Kohama, J. Ye, Y. Kasahara, Y. Nakagawa, M. Onga, M. Tokunaga, T. Nojima *et al.*, Nat. Phys. **12**, 144 (2016).

[31] M. S. El-Bana, D. Wolverson, S. Russo, G. Balakrishnan, D. M. Paul, and S. J. Bending, Supercond. Sci. Technol. **26**, 125020 (2013).

[32] D. B. Haviland, Y. Liu, and A. M. Goldman, Phys. Rev. Lett. **62**, 2180 (1989).

[33] K. E. Wagner, E. Morosan, Y. S. Hor, J. Tao, Y. Zhu, T. Sanders, T. M. McQueen, H. W. Zandbergen, A. J. Williams, D. V. West, and R. J. Cava, Phys. Rev. B **78**, 104520 (2008).

[34] L. Fang, P. Y. Zou, Y. Wang, L. Tang, Z. Xu, H. Chen, C. Dong, L. Shan, and H. H. Wen, Sci. Technol. Adv. Mater. **6**, 736 (2005).

[35] L. Li, X. Deng, Z. Wang, Y. Liu, and M. Abeykoon, npj Quant. Mater. **2**, 11 (2017).

[36] G. Kresse and J. Furthmüller, Phys. Rev. B **54**, 11169 (1996).

[37] G. Kresse and J. Furthmüller, Comput. Mater. Sci. **6**, 15 (1996).

[38] F. Di Salvo, R. Schwall, T. Geballe, F. Gamble, and J. Osiecki, Phys. Rev. Lett. **27**, 310 (1971).

[39] L. Mattheiss, Phys. Rev. B **8**, 3719 (1973).

[40] N. Marzari, A. A. Mostofi, J. R. Yates, I. Souza, and D. Vanderbilt, Rev. Mod. Phys. **84**, 1419 (2012).

[41] M. Farjam, arXiv:1504.04937.

[42] V. Popescu and A. Zunger, Phys. Rev. B **85**, 085201 (2012).

[43] Y. W. Li, J. Jiang, H. F. Yang, D. Prabhakaran, Z. K. Liu, L. X. Yang, and Y. L. Chen, Phys. Rev. B **97**, 115118 (2018).

[44] O. R. Albertini, A. Y. Liu, and M. Calandra, Phys. Rev. B **95**, 235121 (2017).

[45] W. McMillan, Phys. Rev. **167**, 331 (1968).

[46] Y. Wang and A. V. Chubukov, Phys. Rev. B **92**, 125108 (2015).

[47] See Supplemental Material at http://link.aps.org/supplemental/10.1103/PhysRevB.98.035203 for further details, which includes Refs. [36,37,45,48,49,57–67].

[48] R. Hlubina and T. M. Rice, Phys. Rev. B **51**, 9253 (1995).

[49] A. Jacko, J. Fjærestad, and B. Powell, Nat. Phys. **5**, 422 (2009).

[50] S. C. Barrera, M. R. Sinko, D. P. Gopalan, N. Sivadas, K. L. Seyler, K. Watanabe, T. Taniguchi, A. W. Tsen, X. Xu, D. Xiao *et al.*, Nat. Commun. **9**, 1427 (2018).

[51] J. M. Kosterlitz and D. J. Thouless, J. Phys. C: Solid State Phys. **6**, 1181 (1973).

[52] W. Ku, T. Berlijn, and C.-C. Lee, Phys. Rev. Lett. **104**, 216401 (2010).

[53] C.-H. Lin, T. Berlijn, L. Wang, C.-C. Lee, W.-G. Yin, and W. Ku, Phys. Rev. Lett. **107**, 257001 (2011).

[54] O. Rubel, A. Bokhanchuk, S. J. Ahmed, and E. Assmann, Phys. Rev. B **90**, 115202 (2014).

[55] A. Togo and I. Tanaka, Scr. Mater. **108**, 1 (2015).

[56] A. Schlicht, M. Schwenker, W. Biberacher, and A. Lerf, J. Phys. Chem. B **105**, 4867 (2001).

[57] J. Wilson and A. Yoffe, Adv. Phys. **18**, 193 (1969).

[58] L. Benfatto, A. Toschi, S. Caprara, and C. Castellani, Phys. Rev. B **66**, 054515 (2002).

[59] A. A. Golubov and A. E. Koshelev, Phys. Rev. B **68**, 104503 (2003).

[60] N. Volkenshtein, V. Dyakina, and V. Startsev, Phys. Status Solidi B **57**, 9 (1973).

[61] J. M. Ziman, *Electrons and Phonons: The Theory of Transport Phenomena in Solids* (Oxford University Press, New York, 1960).

[62] F. Flicker and J. van Wezel, Phys. Rev. B **94**, 235135 (2016).

[63] A. Rosch, Phys. Rev. Lett. **82**, 4280 (1999).

[64] P. E. Blöchl, Phys. Rev. B **50**, 17953 (1994).

[65] J. P. Perdew, K. Burke, and M. Ernzerhof, Phys. Rev. Lett. **77**, 3865 (1996).

[66] A. A. Mostofi, J. R. Yates, Y.-S. Lee, I. Souza, D. Vanderbilt, and N. Marzari, Comput. Phys. Commun. **178**, 685 (2008).

[67] D. E. Moncton, J. D. Axe, and F. J. DiSalvo, Phys. Rev. B **16**, 801 (1977).